SCIENCE CHINA
Information Sciences

• RESEARCH PAPER •
Special Issue

August 2012 Vol. 55 No. 8: 1801–1815
doi: 10.1007/s11432-012-4634-3

Experimental results and analysis of sparse microwave imaging from spaceborne radar raw data

JIANG ChengLong[1,2,3*], ZHANG BingChen[1,2], ZHANG Zhe[1,2,3], HONG Wen[1,2] & WU YiRong[1,2]

[1]*Science and Technology on Microwave Imaging Laboratory, Beijing* 100190*, China;*
[2]*Institute of Electronics, Chinese Academy of Sciences, Beijing* 100190*, China;*
[3]*Graduate University of Chinese Academy of Sciences, Beijing* 100190*, China*

Received December 12, 2011; accepted May 13, 2012

Abstract Sparse microwave imaging is a novel radar framework aiming to bring revolutions to the microwave imaging according to the theory of sparse signal processing. As compressive sensing (CS) is introduced to synthetic aperture radar (SAR) imaging in recent years, the current SAR sparse imaging methods have shown their advantages over the traditional matched filtering methods. However, the requirement for these methods to process the compressed range data results in the increase of the hardware complexity. So the SAR sparse imaging method that directly uses the raw data is needed. This paper describes the method of SAR sparse imaging with raw data directly, presents the analysis of the signal-to-noise ratio (SNR) in the echo signal by combining the traditional radar equation with the compressive sensing theory, and provides the tests on 2-D simulated SAR data. The simulation results demonstrate the validity of the SNR analysis, and the good performance of the proposed method while a large percentage of the raw data is dropped. An experiment with RadarSat-1 raw data is also carried out to show the feasibility of processing the real SAR data via the method proposed in this paper. Our method is helpful for designing new SAR systems.

Keywords sparse microwave imaging, synthetic aperture radar (SAR) imaging, compressive sensing, signal-to-noise ratio, raw data

Citation Jiang C L, Zhang B C, Zhang Z, et al. Experimental results and analysis of sparse microwave imaging from spaceborne radar raw data. Sci China Inf Sci, 2012, 55: 1801–1815, doi: 10.1007/s11432-012-4634-3

1 Introduction

Synthetic aperture radar (SAR) is an advanced remote sensing equipment for earth observation [1]. Up to now, SAR has made remarkable headway in increasing the imagery resolution and swath width. The most popular SAR imaging methods are based on matched filtering such as the range doppler algorithm (RDA) and the chirp scaling algorithm (CSA) [2,3]. According to the Nyquist theroem, with the lasting demand for higher resolution and wider swath on spaceborne SAR, high speed ADC and dense spatial sampling are required. As a result, the raw data increases dramatically thus bringing great pressure to the limited satellite onboard memory and down-link data rate.

*Corresponding author (email: chenglong.j@gmail.com)

Sparse microwave imaging is a new and promising framework for future microwave imaging. It serves to combine microwave imaging with the theory of sparse signal processing to generate brand-new remote sensing strategy and enable SAR to have better performance in resolution and swath. The state-of-art sparse signal processing theory is compressive sensing (CS), which is a set of sampling and recovery theories that guarantee the reconstruction of a sparse signal from limited samples [4–6]. The CS theory is introduced to radar signal processing for the first time in [7], which indicates that there is no need of pulse compression for the echo signal and the sampling rate can be lower than Nyquist rate. Ref. [9] focuses on spotlight mode SAR and inverse SAR (ISAR). A new SAR modality is proposed together with some applications based on CS. And Ref. [10] proposes the stripmap SAR imaging scheme based on CS. Ref. [11] describes an alternative CS based imaging method with range compressed data and presents the experimental result with ESA data. Ref. [12] demonstrates that emitting a series of irrelevant signals and using CS based recovery algorithm helps to improve the imagery resolution. Ref. [13] proposes a multi-channel SAR imaging method based on distributed compressive sensing (DCS) to reduce the data redundancy among different channels. As a conclusion, the current SAR sparse imaging methods based on CS improve the radar ability and image quality.

However, the fact that the requirement for these methods to process the compressed range data would simultaneously increase the hardware complexity, is the main obstacle for designing a new spaceborne SAR scheme which is expected to reduce the pressure on transmitting the raw data. So the SAR sparse imaging method that directly uses the raw data is needed. The contribution of this paper is developing a new SAR imaging method for directly processing the raw data via CS. This paper constructs the observation model, implements the parameters, presents the analysis of the signal-to-noise ratio (SNR) in the echo signal by combining the traditional radar equation with the compressive sensing theory, and provides the tests on 2-D simulated SAR data. The simulation results demonstrate the validity of the SNR analysis, and exhibit good performance of the proposed method while a fairly large percentage of the raw data is dropped. An experiment with RadarSat-1 raw data is also carried out to show the feasibility of processing the real SAR data via the method proposed in this paper, and it is shown that our method helpful to the designation for new SAR systems.

The reminder of this paper is organized as follows. The fundamentals of CS theory is reviewed in Section 2. In Section 3, the SAR sparse imaging method with the raw data via CS is described in detail. Then, the tests with 2-D simulated raw data are presented in Section 4, aiming to validate the SNR analysis and the method proposed in this paper. An experiment with RadarSat-1 raw data is also carried out to show the feasibility of processing the real SAR data via the proposed method. In Section 5, we provide the conclusion.

2 Preliminary: the compressive sensing theory

This section briefly discusses the theoretical fundamentals of CS theory [4–6]. Consider a signal $x \in \mathbb{R}^{N\times 1}$, which has a sparse representation in some basis $\boldsymbol{\Psi} = [\psi_1 \mid \psi_2 \mid \cdots \mid \psi_N]$,

$$x = \sum_{n=1}^{N} \psi_n \alpha_n = \boldsymbol{\Psi}\alpha, \tag{1}$$

where α is an $N \times 1$ column vector of weighting coefficients $\alpha_n = \langle x, \psi_n \rangle$. If there are only $K(K \ll N)$ of the coefficients α_n to be nonzero, x is called sparse in the $\boldsymbol{\Psi}$ domain with K sparsity. The procedure of acquiring the measurement of x is as follows:

$$y = \boldsymbol{\Phi}x + \epsilon, \tag{2}$$

where $\boldsymbol{\Phi} \in \mathbb{R}^{M\times N}$ is the observation matrix, $y \in \mathbb{R}^{M\times 1}$ is the measurement, and $\epsilon \in \mathbb{R}^{M\times 1}$ is the measurement noise. Since $M < N$, x cannot be recovered directly from y, by substituting x with (1), y can be written as

$$y = \boldsymbol{\Phi}x + \epsilon = \boldsymbol{\Phi}\boldsymbol{\Psi}\alpha + \epsilon. \tag{3}$$

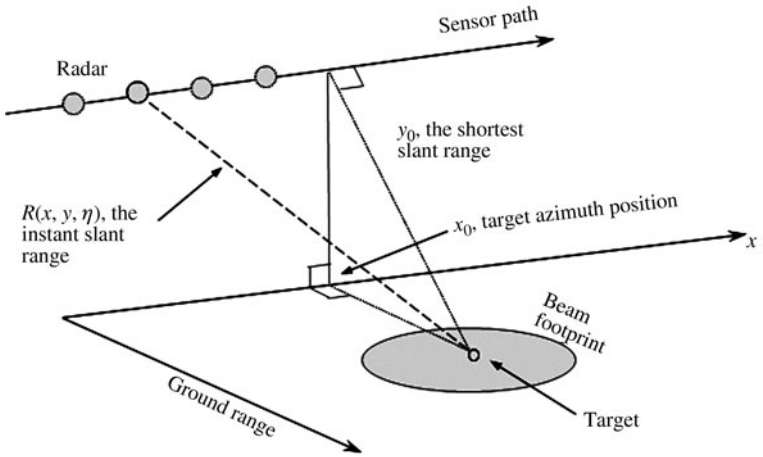

Figure 1 The stripmap SAR geometry.

Because α in (3) has K sparsity, and $K < M < N$, the coefficients in α could be solved from an optimization problem:

$$\min_{\alpha} \|\alpha\|_1 \text{ s.t. } \|y - \boldsymbol{\Phi\Psi}\alpha\|_2 \leqslant \xi, \tag{4}$$

where $\xi = \|\epsilon\|_2$. The signal x can then be reconstructed from α. When the measurement matrix $\boldsymbol{\Phi\Psi}$ satisfies restricted isometry property (RIP) conditions [14], the sparse vector α can be recovered perfectly. Up to now, (4) can be solved with different kinds of optimization methods [15–17], and in this paper, we use the iterative shrinkage/thresholding algorithm (IST) [17,18] as the recovery algorithm.

3 Framework of SAR sparse imaging from raw data

This section describes the method of SAR sparse imaging based on CS in detail. The expression of the echo signal is introduced after reviewing the stripmap SAR geometry. From this expression, we build the observation model and implement the model parameters. Then, the analysis on the SNR of the echo signal is presented. At the end of this section, we present a brief comparison of three different imaging methods.

3.1 Stripmap SAR imaging geometry

We start with describing the framework of SAR sparse imaging from raw data by taking the stripmap SAR mode for example because that it is one of the most widely used SAR modes. To stripmap SAR, the radar antenna points to the target scene at a certain look angle, transmits the EM pulses and receives the successive echoes from the target scene in every time interval called pulse repetition interval (PRI). As the radar sensor moves along the flight path, the beam footprint becomes a strip. The simplified geometry of the spaceborne stripmap SAR is shown in Figure 1.

The signal used in stripmap SAR is usually a linear frequency modulation (LFM) signal. For convenience, we assume that the baseband form of the transmitted signal is an LFM singal:

$$p(\tau) = \text{rect}\left(\frac{\tau}{T_p}\right) \exp\{\text{j}\pi K_r \tau^2\}, \tag{5}$$

where τ is the fast time; K_r is the chirp rate; T_p denotes time duration of the pulse; and rect$(\cdot)$ stands for the unit rectangular function. The echo from a point target can be written as

$$s(\tau, \eta) = \sigma_0 w_a\left(\eta - \frac{x_0}{v_{rc}}\right) \exp\left\{-\text{j}4\pi f_0 \frac{\sqrt{y_0^2 + (v_{rc}\eta)^2}}{\text{c}}\right\} \times p\left(\tau - \frac{\sqrt{y_0^2 + (v_{rc}\eta)^2}}{\text{c}}\right), \tag{6}$$

where η is the azimuth time; x_0 is the azimuth position of a target; σ_0 is the backscattering coefficient of the point target; $w_a(\cdot)$ is the azimuth weighting function; f_0 is the carrier frequency; y_0 is the shortest slant range of target when $\eta = 0$; v_{rc} is the equivalent platform velocity; c is speed of light.

When observing a certain scene C, the echo signal can be written in the form of double integrals:

$$s(\tau,\eta) = \iint\limits_{(x,y)\in C} \sigma(x,y)\cdot w_a\left(\eta - \frac{x}{v_{rc}}\right)\exp\left\{-\mathrm{j}4\pi f_0\frac{R(x,y,\eta)}{\mathrm{c}}\right\}\cdot p\left(\tau - \frac{R(x,y,\eta)}{\mathrm{c}}\right)\mathrm{d}x\mathrm{d}y, \tag{7}$$

where C is the observation scene, $R(x,y,\eta) = \sqrt{y^2 + (v_{rc}\eta - x)^2}$ is the instant slant range between the target at (x,y) and the radar platform at azimuth time η; y is the shortest slant range of target at (x,y). In order to have a simple expression, we set

$$\theta(x,y,\tau,\eta) \doteq w_a\left(\eta - \frac{x}{v_{rc}}\right)\exp\left\{-\mathrm{j}4\pi f_0\frac{R(x,y,\eta)}{\mathrm{c}}\right\}\cdot p\left(\tau - \frac{R(x,y,\eta)}{\mathrm{c}}\right). \tag{8}$$

Below we will derive the observation model.

3.2 The observation model

Eq. (7) reveals how the echo signal responds to the observation scene. In the derivation of the observation model, we need to discrete the echo signal and the observation scene. Here, we discuss the discretization of both of them from the mathematical point of view, and on this basis, we give a concrete form of the observation model. The details of the parameters in the model will be presented in the next subsection.

The first step in our derivation of the observation model is to discrete the observation scene. In the application of remote sensing, the imaging terrain is continuous, which means that at each location of the terrain there exists a corresponding backscattering coefficient. So the procedure of discreting the observation scene C is dividing it into many "small" units C_n $(n = 1, 2, \ldots, N)$ and then choosing a proper value as the backscattering coefficient for each unit.

$$s(\tau,\eta) = \sum_{n=1}^{N}\iint\limits_{C_n}\sigma(x,y)\cdot\theta(x,y,\tau,\eta)\mathrm{d}x\mathrm{d}y, \tag{9}$$

where C_n satisfies $C = \bigcup_n C_n$, $\bigcap_n C_n = \emptyset$. Using an average value of the backscattering coefficient $\bar{\sigma}t[x_n, y_n]$ in C_n, we have

$$s(\tau,\eta) = \sum_{n=1}^{N}\bar{\sigma}[x_n,y_n]\cdot\iint\limits_{C_n}\theta(x,y,\tau,\eta)\mathrm{d}x\mathrm{d}y. \tag{10}$$

Since $\theta(x,y,\tau,\eta)$ is a smooth and continuous function on (x,y), according to the mean value theorem for integration, there exists a point (x_n, y_n) in C_n such that $\theta(x_n,y_n,\tau,\eta)\cdot\|C_n\| = \iint_{C_n}\theta(x,y,\tau,\eta)\mathrm{d}x\mathrm{d}y$, where $\|C_n\|$ is the size of C_n. Then

$$s(\tau,\eta) = \sum_{n=1}^{N}\bar{\sigma}[x_n,y_n]\cdot\theta(x_n,y_n,\tau,\eta)\cdot\|C_n\|. \tag{11}$$

The next step in the derivation of the observation model is to discrete the echo signal. The acquisition of the echo signal can be generally described as follows. First of all, the receiving time sequence is divided into a number of time slices. In each time slice, the receiving antenna weights the echo with a certain function, and then at a certain moment within each slice, the system captures and records the signal level and stores it in the memory. Following this kind of sampling scheme, we divide the time sequence into T_m $(m = 1, 2, \ldots, M)$, where $T = \bigcup_m T_m$, $\bigcap_m T_m = \emptyset$. Then we use a weighting function $h_m(\tau,\eta)$ to modulate the echo signal and sample the signal level at $(\tau_m, \eta_m t)$. The result can be expressed as

$$s[\tau_m,\eta_m] = \sum_{m=1}^{M}\sum_{n=1}^{N}\phi(m,n)\cdot\bar{\sigma}[x_n,y_n], \tag{12}$$

where $\phi(m,n)$ reads

$$\phi(m,n) \doteq \|C_n\| \cdot \iint\limits_{T_m} \theta(x_n, y_n, \tau, \eta) \cdot h_m(\tau, \eta.)\mathrm{d}\tau\mathrm{d}\eta. \tag{13}$$

Especially, when $h_m(\tau,\eta) = \delta(\tau_m, \eta_m)$, we have

$$\phi(m,n) \doteq \|C_n\| \cdot \theta(x_n, y_n, \tau_m, \eta_m). \tag{14}$$

After downsampling in both the range and azimuth directions, we add the additive noise to (12) to accomplish the observation model, which can be written as

$$Y = \Phi X + E, \tag{15}$$

where $Y \in \mathbb{C}^{M\times 1}$ is the echo signal vector; $X \in \mathbb{C}^{N\times 1}$ is the target vector; $E \in \mathbb{C}^{M\times 1}$ denotes the additive noise vector; $\Phi = \{\phi(m,n)\}_{M\times N}$ is the measurement matrix.

3.3 Implementation of the model parameters

First we build the observation model of the stripmap mode SAR from a mathematical point of view and here we specify every parameter in this model, so that a connection can be established from the perspective of radar.

For an easier understanding of all the parameters, we start with describing the structure of the SAR echo data and assume that the radar has zero side-look angle. In the stripmap mode SAR system, the echo data is collected like this: the sensor moves along the path, carrying out the spatial sampling in each PRI. Every spatial sampling lasts a certain period of time. During this time, it captures the echo signal uniformly at a βB_r sampling rate, where β stands for the over-sampling rate, and B_r is the bandwidth of the transmitted signal $p(\tau)$. All the sampling processes meet the requirements of the Nyquist sampling theorem.

According to this type of sampling strategy, each time slice T_m has the same size, assumed to be ΔT. The adjacent T_m are separated by the interval $\frac{1}{\beta B_r}$. As the echo signal is usually expressed in a two-dimensional form, we divide the points of the echo signal M into two parts: the azimuth and the range part, namely $M = M_a \cdot M_r$, where M_a are the azimuth sampling points, M_r are the range sampling points. A single azimuth observation lasts M_r pieces of T_m, and so the corresponding range distance is $\frac{M_r}{\beta B_r}$, and the total observation time is $\frac{M_a M_r}{\beta B_r} = \frac{M}{\beta B_r}$.

The radar image acquired by applying traditional SAR imaging algorithm to the echo data is a two-dimensional datum in azimuth and slant-range direction. Including the incomplete aperture part, its total number of points is $N = N_a N_r = M$, in which the azimuth points N_a equal M_a, and the slant range points N_r equal M_r. Intuitively, the numerical value of every point in the image data can be considered to be the average backscattering coefficient of the corresponding discrete scene C_n. Moreover, the size of all the discrete scene C_n are identical, $\|C_n\| = \Delta x \Delta y = \frac{cV_{rc}\mathrm{PRI}}{2\beta B_r}$, where $\Delta x = V_{rc}\mathrm{PRI}$, $\Delta y = \frac{c}{2\beta B_r}$.

From the analysis above we can see that the the parameter of the discrete scene is not only related with the scheme of stripmap mode SAR itself, but with the way of the echo data acquisition as well. Before giving the specific parameter settings of our observation model, it is useful to assume that the observation region has a rectangular shape and the echo reflected outside of the observation region is a clutter echo. The schematic arrangement of the discrete scene is shown in Figure 2.

In our model, no doubt the new sampling methods (e.g., the jittered undersampling method [20]) can be applied to the echo data acquisition [9,19]. However, for the sake of convenience, we add a "downsampling" process to the traditional echo data acquisition method, which can be expressed as

$$Y = H(\Phi X + E) = \Phi' X + E', \tag{16}$$

where the construction of Φ and X refer to the aforementioned methods; $\Phi' \in \mathbb{C}^{M'\times N}$ and $E' \in \mathbb{C}^{M'\times 1}$ are the new observation matrix and noise vector, respectively; $H \in \mathbb{C}^{M'\times M}$ is the downsampling matrix. Currently, there are three kinds of downsampling strategy available: the uniform downsampling, the random downsampling and the random demodulation downsampling. As these names imply, the uniform

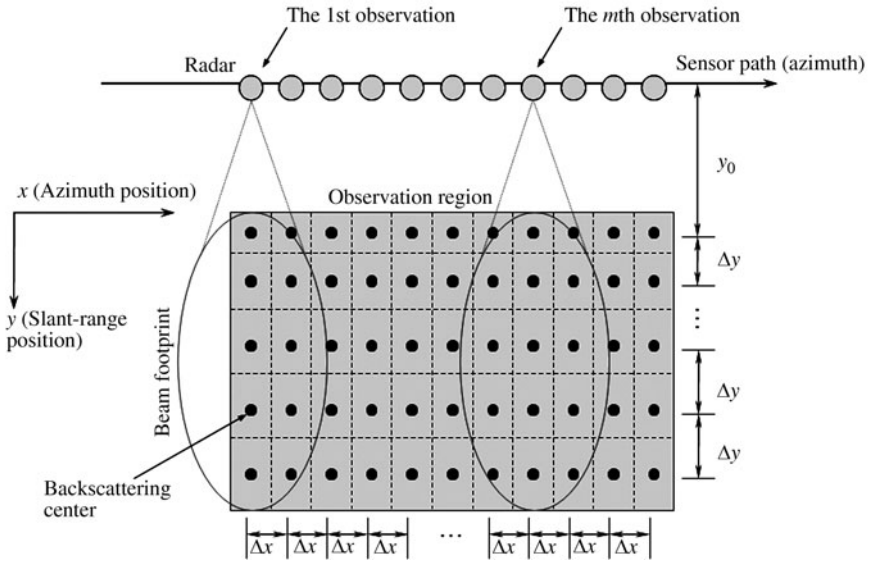

Figure 2 Illustration of the arrangement for the discrete scene in slant-range plane.

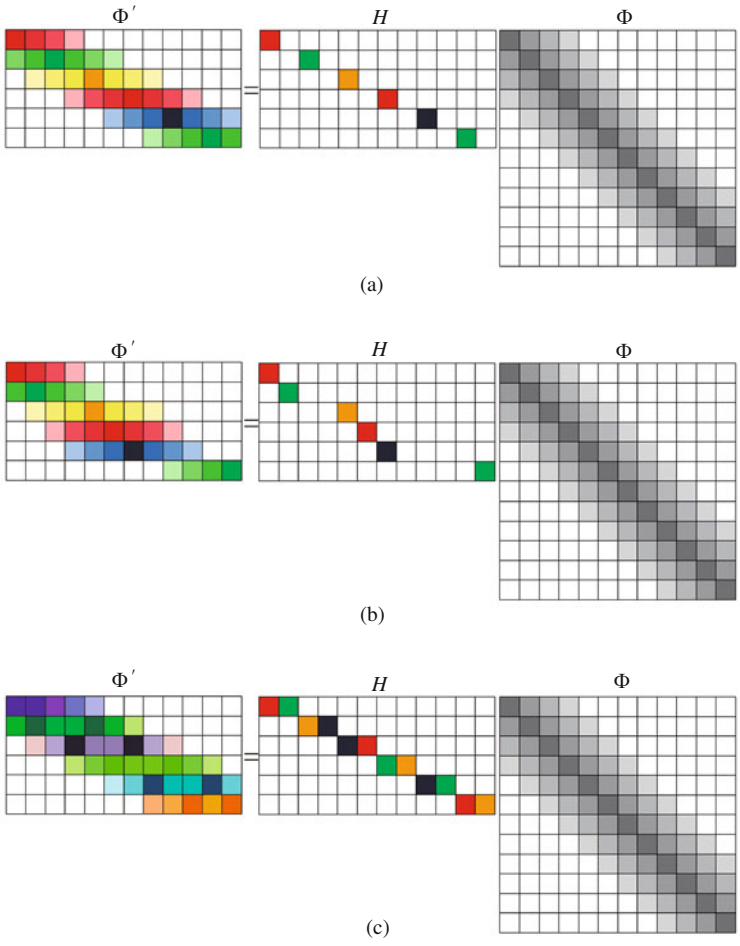

Figure 3 Illustration of the downsampling Matrix H, with 50% rows of the observation matrix selected. (a) The diagram of the uniform downsampling matrix which uniformly selects 50% of the rows; (b) the diagram of the random downsampling matrix which randomly selects 50% of the rows; (c) the diagram of the random demodulation downsampling matrix which sums up every two rows with randomly generated sequence each time.

downsampling matrix selects the rows of the observation matrix with uniform interval; the random downsampling matrix selects the rows randomly; the random demodulation downsampling matrix selects certain rows of the observation matrix each time and sums them up with randomly generated weighting sequence. Figure 3 shows the pattern of the three kinds of downsampling matrix.

3.4 The recovery algorithm

When Φ' satisfies certain conditions and SNR is high enough, the target vector X can be exactly reconstructed by solving the following regularization problem with convex methods:

$$\min_{\widehat{X}} \lambda\|\widehat{X}\|_1 + \|Y - \Phi'\widehat{X}\|_2^2, \tag{17}$$

where λ controls the shrinkage extent. In most cases, the statistics of noise are unknown and need to be estimated. So we use a denoising method based on IST [17,18] to solve (17).

An important step of the algorithm is to select a proper estimated thresholder, which can be used to control the sparsity of the target vector X. Since the exact value of the sparsity is unknown, we suggested setting it to an approximately larger value so that the altered IST algorithm converges a closer solution to the real target scene.

3.5 SNR analysis

In this subsection, we present an overview of the radar equation, combine it with the theory of CS, and provide an SNR expression for the CS based method. According to the traditional radar equation [1], in the point target case, the traditional SNR of the echo signal is

$$\mathrm{SNR}_{\mathrm{trad}} = \frac{P_s}{kF_{op}T_sB_n} = \frac{P_tG^t\rho A_e}{(4\pi R^2)^2 kF_{op}T_sB_n}, \tag{18}$$

where P_s is the received power, k is Boltzmann's constant, $k = 1.38 \times 10^{-23}$J/K; F_{op} is the operating noise factor and T_s is the total source equivalent noise temperature, B_n is the bandwidth of the receiver, chosen just wide enough to pass the signal, but no more wider, and G^t is the transmitting gain. ρ is the radar scattering cross section of a target. The inferred cross section ρ is the product of the relative backscatter coefficient σ and the geometry area ΔS, $\rho = \sigma \cdot \Delta S$. For a receiving antenna, the effective aperture is $A_e = \lambda^2 G^r/4\pi$, where G^r is the receiving gain.

For a distributed target, the traditional radar equation becomes

$$\mathrm{SNR}_{\mathrm{trad}} = \frac{P_t \int [G^t(\theta,\phi)\rho(\theta,\phi)A_e(\theta,\phi)/(4\pi R^2)^2]\mathrm{d}\theta\mathrm{d}\phi}{kF_{op}T_sB_n}. \tag{19}$$

It is useful to assume that the distributed target has isotropic mean backscatter coefficient over the scene and that it remains the same for every position of the antenna. So the cross section becomes a constant $\overline{\rho}$, and (19) can be simplified into

$$\mathrm{SNR}_{\mathrm{trad}} = \frac{P_t\overline{\rho}\lambda^2}{(4\pi)^3 kF_{op}T_sB_n} \int \frac{G^t(\theta,\phi)G^r(\theta,\phi)}{R^4}\mathrm{d}\theta\mathrm{d}\phi. \tag{20}$$

In a single cell case, the $\mathrm{SNR}_{\mathrm{trad}}$ is expressed as

$$\mathrm{SNR}_{\mathrm{trad}}^{\mathrm{cell}} = \frac{P_tG^2\overline{\rho}\lambda^2\Delta p\Delta R_g}{(4\pi)^3 R^4 kF_{op}T_sB_n}, \tag{21}$$

where Δp is the extension distance in azimuth and ΔR_g is the extension distance in ground range.

According to [21], the SNR in (15) can be defined as

$$\mathrm{SNR}_{\mathrm{cs}} = \frac{\|\Phi X\|_2^2}{\|E\|_2^2}. \tag{22}$$

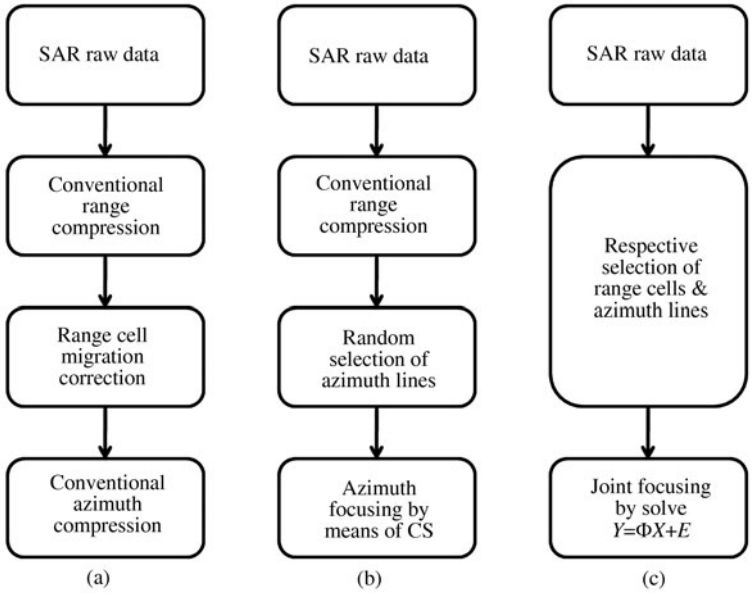

Figure 4 Flowchart of the three imaging methods. (a) Basic RDA; (b) SAR imaging method mentioned in [11]; (c) SAR sparse imaging method proposed in this paper.

Assume that the antenna receives an entire aperture of the echo signal, and there is no downsampling. Then in a single cell case, the SNR can be expressed as

$$\overline{\mathrm{SNR}}_{\mathrm{cs}}^{\mathrm{j}} = \frac{E(\|\Phi_{ij}x_j\|_2^2)}{E(\|N_i\|_2^2)} = \frac{P_t G^t \rho_j A_e}{(4\pi R^2)^2 k F_{op} T_s B_n}, \tag{23}$$

where $E(\cdot)$ stands for the expectation. In average meaning, we have

$$\overline{\mathrm{SNR}}_{\mathrm{cs}}^{\mathrm{cell}} = \frac{P_t G^t \overline{\rho} A_e}{(4\pi R^2)^2 k F_{op} T_s B_n}. \tag{24}$$

For a K-point target scene, if all of the points are independent, then

$$\overline{\mathrm{SNR}}_{\mathrm{cs}} = \frac{E(\|\Phi X\|_2^2)}{E(\|N\|_2^2)} = \frac{E(\sum_i \|\sum_j \Phi_{ij}x_j\|_2^2)}{E(\sum_i \|N_i\|_2^2)} = \sum_j \frac{\sum_i E(\|\Phi_{ij}x_j\|_2^2)}{\sum_i E(\|N_i\|_2^2)} = \sum_j \overline{\mathrm{SNR}}_{\mathrm{cs}}^{\mathrm{j}}. \tag{25}$$

Especially, in average meaning, (25) can be rewritten as

$$\overline{\mathrm{SNR}}_{\mathrm{cs}} = K \cdot \overline{\mathrm{SNR}}_{\mathrm{cs}}^{\mathrm{cell}}. \tag{26}$$

If the K scatters do not distribute independently, then we use RIP to analyze SNR. If Φ satisfies $\mathrm{RIP}(N, K, \delta)$ for every K-sparse vector X, then we have

$$(1-\delta)\|X\|_2^2 \leqslant \|\Phi X\|_2^2 \leqslant (1+\delta)\|X\|_2^2; \tag{27}$$

Moreover, if the amplitudes of the K scattering points are independent, and the noise is white and independent of the signal as well, then we have

$$(1-\delta)\frac{E(\|X\|_2^2)}{E(\|N\|_2^2)} \leqslant \overline{\mathrm{SNR}}_{\mathrm{cs}} \leqslant (1+\delta)\frac{E(\|X\|_2^2)}{E(\|N\|_2^2)}. \tag{28}$$

For a distributed target, it is appropriate to define the radar cross section per unit geometrical area of the scene as a random variable. The conclusion of the SNR of a distributed target is the same with the K-point target.

Table 1 Key parameters

System parameters	Numerical value
Carrier frequency	5.3 GHz
Band width	8.51 MHz
Pulse duration	11.79 μs
Radar velocity	7062 m/s
Pulse repetition frequency	1256.98 Hz
Azimuth FM rate	1733 Hz/s

3.6 Comparison of the three imaging methods

As is shown in Figure 4, compared with the CS SAR imaging method in [11], the proposed SAR sparse imaging method downsamples the raw data in both azimuth and range direction. The most noticeable advantage of the new method presented is that no preprocessing operations (e.g., range compression and range cell migration correction) are required. As a result, the radar hardware can be simplified.

4 Experimental results

In this section, we provide three sets of simulation and one experiment using the raw data of RadarSat-1. The simulation results verify the analysis of SNR mentioned in the above section and show the performance of our method, with the results of the matched filtering method and the current CS method as comparisons. The experiment result demonstrates that it is feasible to apply our method to the oceanic area of real data.

4.1 The parameters

The procedure of the simulation proceeds in the following steps.

• Step 1. Use the LFM signal as the transmitted signal. The size of the target scene is 64×64 in grids.

• Step 2. Generate the complex backscattering coefficient of each target, of which the amplitude satisfies Rayleigh distribution and the phase satisfies uniform distribution. Moreover, choose the index of each target in the scene randomly.

• Step 3. Generate the observation matrix and the echo signal using the method in the above section, and then add the white Gaussian noise to the echo signal.

Some key parameters are provided in Table 1.

4.2 Simulations

The first set of simulations is carried out in order to verify the analysis of SNR based on CS. In this test, the expectation amplitude of each target equals 0.36 and the white Gaussian noise satisfies $N(0, 1)$. Moreover, we make assumption for the other parameters so that the SNR in the traditional radar equation is simply $\mathrm{SNR}_{\mathrm{trad}} = -4.4$ dB. According to (26), the theoretical SNR is $\mathrm{SNR}_{\mathrm{cs}}^{\mathrm{theory}} = 0.36K + \mathrm{SNR}_{\mathrm{trad}}$ (dB), where K is the number of the target. For each K, we make repeatitions 100 times to get the statistic curve of the SNR based on CS. The result is shown in Figure 5. The theoretical curve is also given as a comparison.

Then, we carry out the second set of simulations to see the performance of our imaging method under different target scenes. In this test, the number of the target ranges from 1 (0.02% of the scene size) to 369 (10% of the scene size), and the SNR of the echo signal ranges from -10 to 20 dB. Besides, we have tested the noiseless scene as well. By adopting the sampling and downsampling strategy mentioned in Section 3, we randomly choose 50% of the azimuth data and 50% of the range data. Then the observation model is changed into problem (17) and solved with the Lq algorithm. The results of the matched filtering method and the current CS method are also provided as comparisons, while the matched filtering method uses all the echo data and the current CS method uses the same 50% azimuth data but full range data.

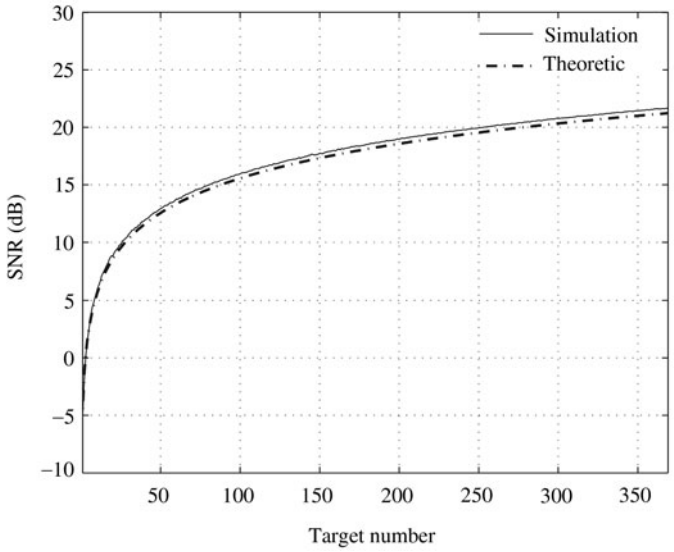

Figure 5 Comparison of the statistic SNR curve (solid line) and the theoretical SNR curve (dotted line) with different target numbers. The two curves are very close to each other. The max error between the two curves is less than 0.5 dB.

Generally, the recovery results show that, all the three methods perform better with higher echo signal SNR. It is empirically observed that our method and the current CS method perform better with sparse target scenes than those without. Moveover, under the same SNR and the scene condition, our method outperforms the others. In this paper, the compared results are summarized by representing three cases (-10 dB, 0 dB and 20 dB with 1% target number) in Figure 6. The three cases show the main tendency of the processed results in this SNR range. Figures 6(a) is the amplitude of the ground truth. The last 9 subfigures are organized as follows. The figures in each row are the results under different SNR (20 dB, 0 dB and -10 dB, from top to bottom); Figures 6(b)(e)(h) are the results processed by the matched filtering method; Figures 6(c)(f)(i) are the results processed by the current CS method; Figures 6(d)(g)(j) are the results processed by the proposed method. From the visual point of view, the latter two methods perform better on denoising and lower sidelobes.

In Figure 7 and Figure 8, the cross sections of the 24th azimuth sample and the 42th range sample are picked out respectively to illustrate these advantages. According to the amplitude, all the three methods successfully recover the ground truth to the accurate position. However, an artifact appears near the 5th sample in Figure 7(a), while it is lower in Figure 7(b) and completely absent in Figure 7(c). Figures 7(a)(b)(c) also show that the sidelobe in the range direction is apparently reduced by means of CS. Moreover, compared with Figure 8(a), the two close targets (targets located near the 25th sample) in the same azimuth direction can be easier distinguished from Figure 7(c).

On the other hand, Figure 9 plots the recovered results in amplitude and phase coordinates. Figure 9(a) shows that the amplitude and phase of the result exhibit a more precise match to the ground truth with high SNR. As is observed in this test, for SNR that is lower than or equal to 0 dB, the error of the phase between the result and the ground truth becomes apparent. This test demonstrates that our method has the ability of phase preservation.

The third set of simulations is carried out to compare the three downsampling methods. In this test, we generate the target scene, the echo signal and the observation matrix, and then use the three downsampling matrix mentioned in Section 3 to down-sample them. The random downsampling matrix randomly selects 50% of the data in azimuth and 50% of the data in range; the uniform matrix uniformly selects 50% of the data in azimuth and 50% of the data in range; and the random demodulation downsampling matrix randomly selects 50% of the data in azimuth and sums up every two rows in the range direction with randomly generated weighting sequence. Then, the reconstruction is applied. The RMSE is used to compare the performance of the methods, where RMSE$=\frac{\|X-\widehat{X}\|}{\|X\|}$. We repeat the test for 200 times with different target scenes to obtain the histograms. Figure 10 shows that the random downsampling matrix has apparently lower RMSE than the other two downsampling methods, and the random demodulation

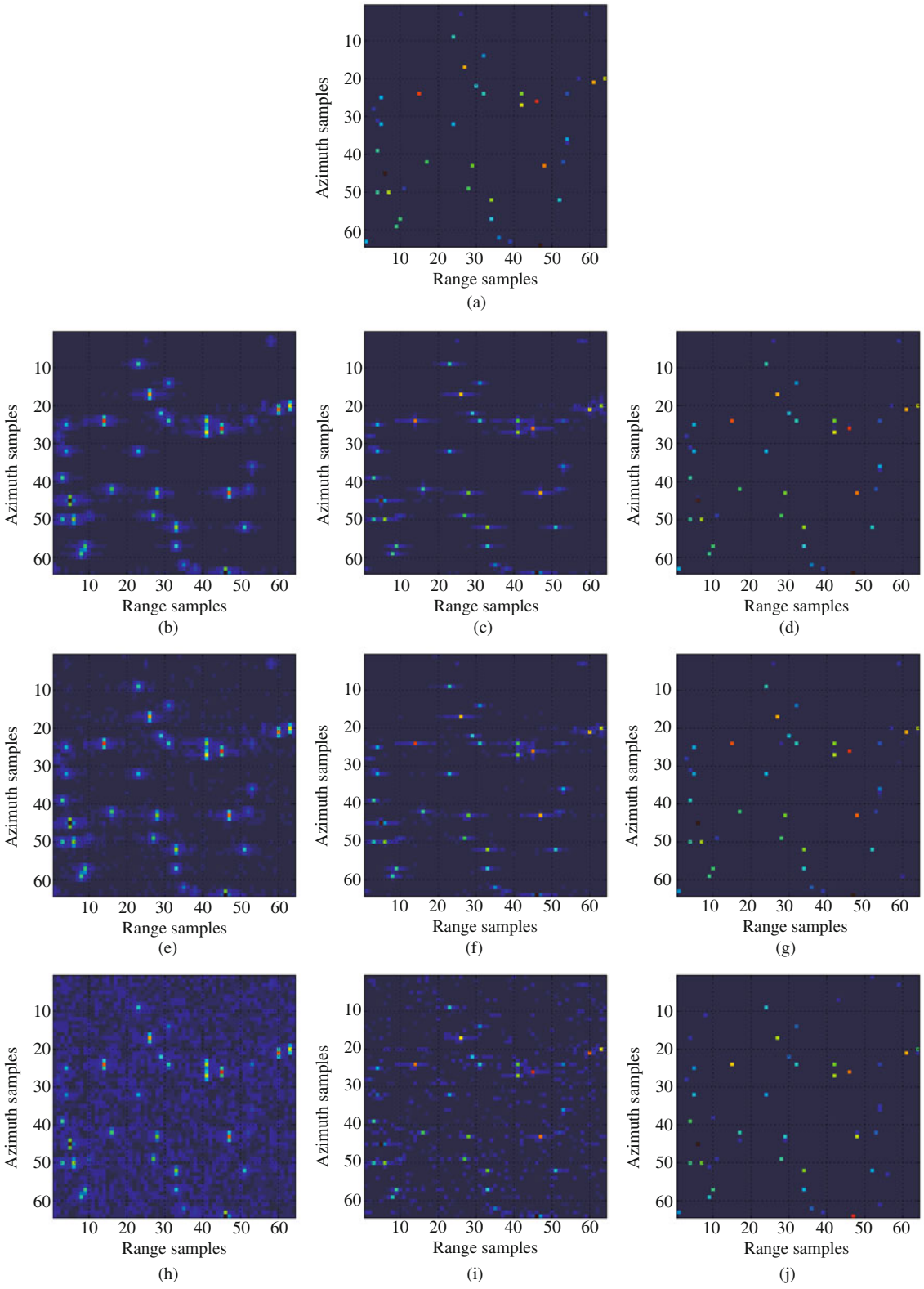

Figure 6 Amplitude retrieved for a simulated scene with forty-one point targets with different SNR levels (20 dB in (b)(c)(d), 0 dB in (e)(f)(g) and −10 dB in (h)(i)(j)). (a) The ground truth; (b)(e)(h) results obtained by the matched filtering method; (c)(f)(i) results obtained by the CS method in [11] with 50% of the azimuth data; (d)(g)(j) results obtained by the proposed method with the same 50% of the azimuth data and 50% of the range data.

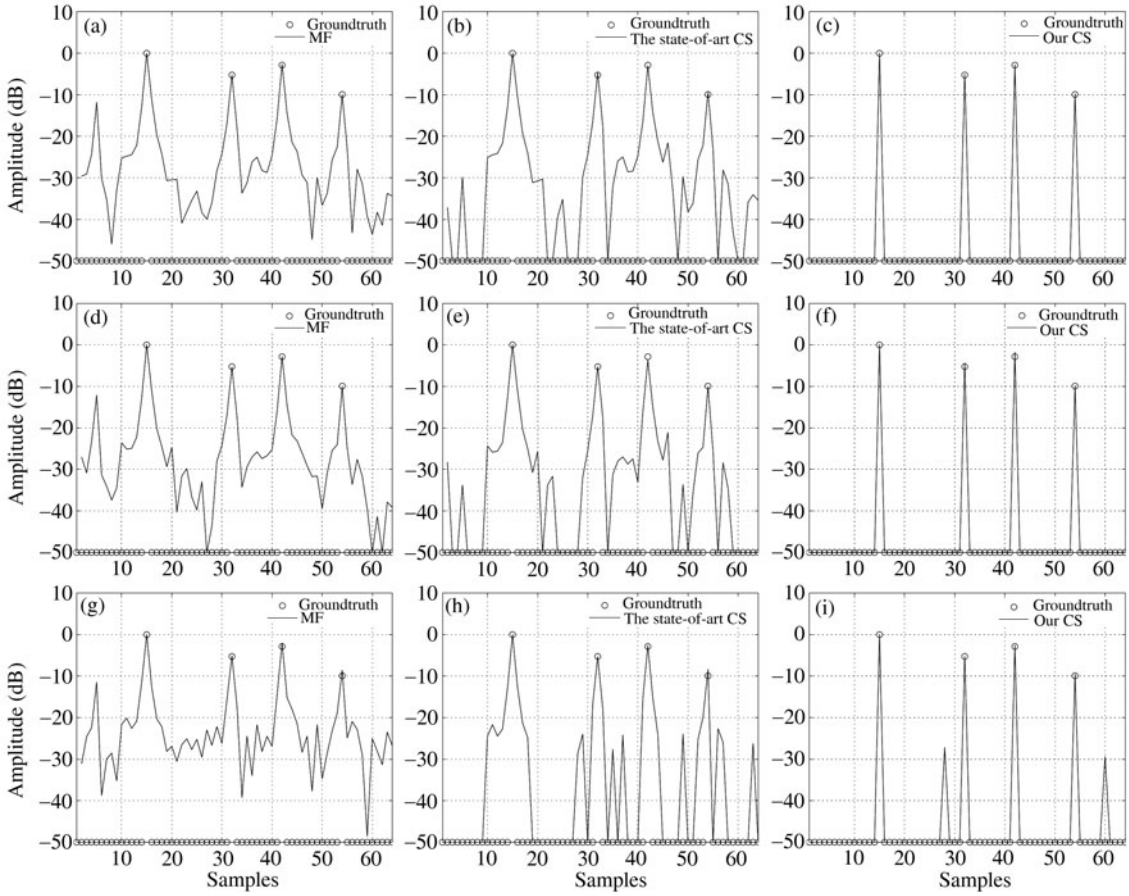

Figure 7 Range cross section (at the 24th azimuth sample) of the amplitude retrieved for the same scene in Figure 6, with different SNR levels (20 dB in (a)(b)(c), 0 dB in (d)(e)(f) and −10 dB in (g)(h)(i)). (a)(d)(g) Results obtained by the matched filtering method; (b)(e)(h) results obtained by the CS method in [11] with 50% of the azimuth data; (c)(f)(i) results obtained by the proposed method with the same 50% of the azimuth data and 50% of the range data.

downsampling matrix is a little better than the uniform downsampling matrix.

4.3 Experimental result of real data

In this section, we provide some experimental results of the raw data of RadarSat-1 sea area. The details of target and data parameters are provided in [2].

Figure 11(a) shows the imaging result via RDA, and Figure 11(b) shows the image of the same area which was imaged using the method proposed in this paper with only 11.1% of the full data (15.4% of the azimuth data and 72.0% of the range data). We can see that there are good focuses and less sidelobes. Although the scene is not exactly sparse, the experiment result shows that it is feasible to process it with the method proposed in this paper.

5 Conclusion

In this paper, we have proposed a novel CS based imaging method for directly processing the raw data. The most noticeable advantage of the new method is that no preprocessing operations (e.g., range compression and range cell migration correction) are required. As a result, the radar hardware can be simplified. Besides, the simulation results with sparse targets show that there are less sidelobes. The proposed method exhibits a better performance while less echo data is collected. An experiment with RadarSat-1 raw data is also carried out. The test scene contains the compressible targets. The acceptable imaging result shows the feasibility of processing the real SAR data using our new method.

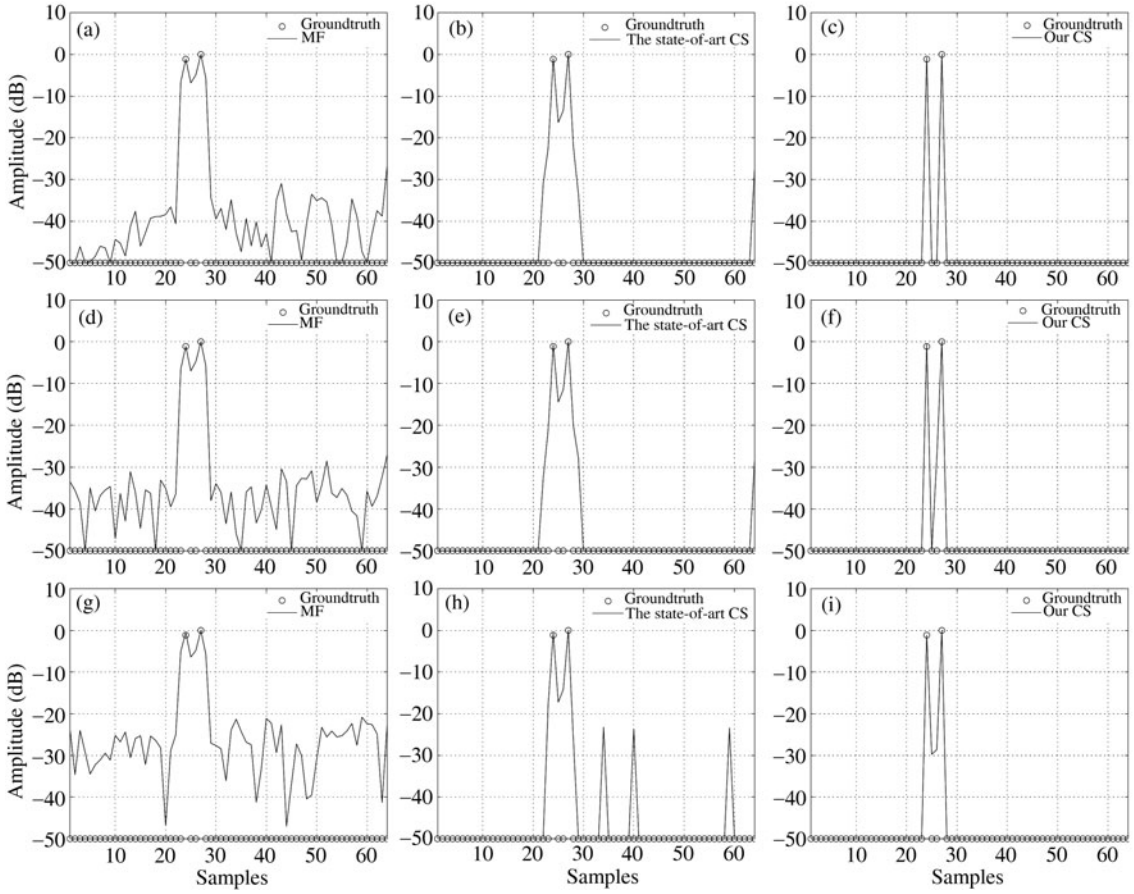

Figure 8 Azimuth cross section (at the 42th range sample) of the amplitude retrieved for the same scene in Figure 6, with different SNR levels (20 dB in (a)(b)(c), 0 dB in (d)(e)(f) and −10 dB in (g)(h)(i)). (a)(d)(g) Results obtained by the matched filtering method; (b)(e)(h) results obtained by the CS method in [11] with 50% of the azimuth data; (c)(f)(i) results obtained by the proposed method with the same 50% of the azimuth data and 50% of the range data.

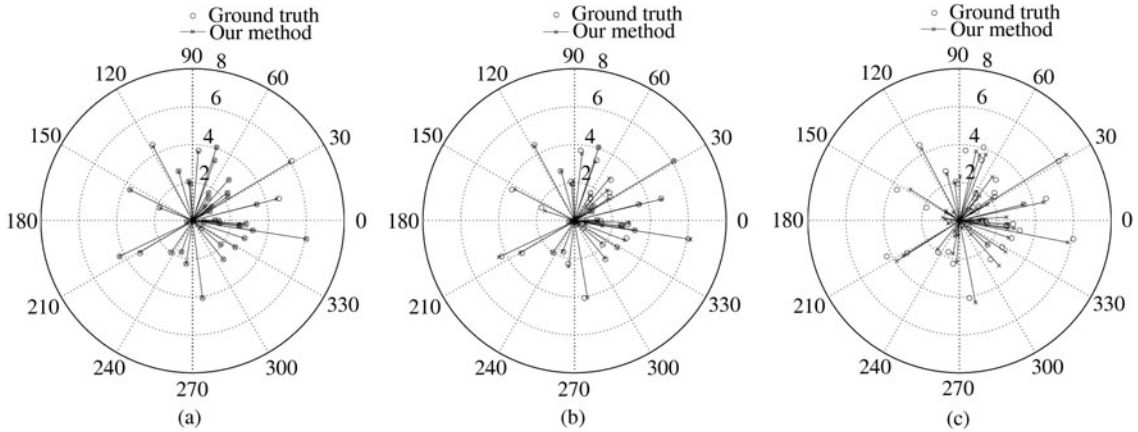

Figure 9 Amplitude and phase retrieved for the same scene in Figure 6, by the means of our method with 50% of the azimuth data and 50% of the range data. (a) SNR=20 dB; (b) SNR=0 dB; (c) SNR=−10 dB.

On the other hand, this paper presents the analysis of the SNR in the echo signal by combining the traditional radar equation with the CS theory. The conclusion is that the echo SNR based on CS is linear with the sparse number of the targets when the targets are independent. The test result with 2-D simulated data demonstrates the validity of the SNR analysis, which in turns provides a theoretical guarantee for the recovery quality by the proposed method when the traditional SNR is usually at a low level.

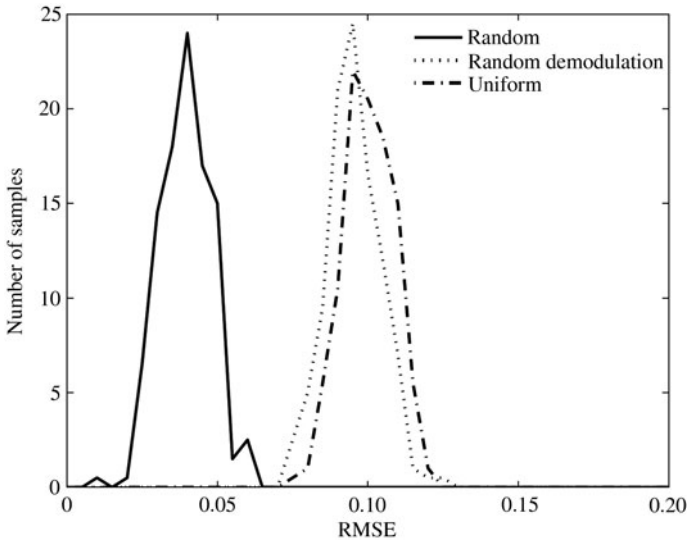

Figure 10 Histograms of the RMSE introduced by the proposed method, with different sampling methods, SNR= 20 dB.

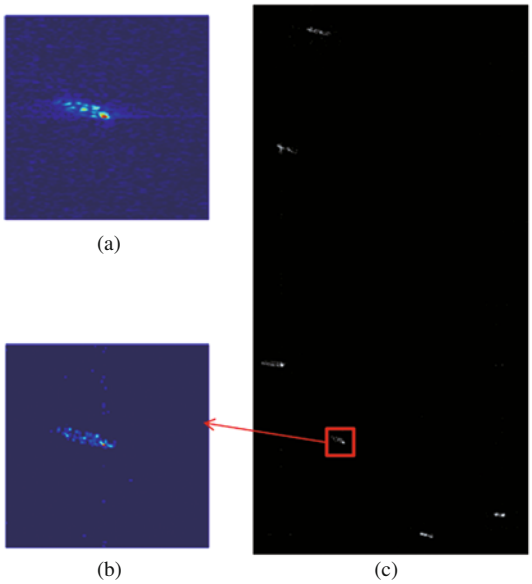

Figure 11 RadarSat-1 raw data imaging results. (a) The imaging result of a ship by RDA; (b) the imaging result of a ship by the method proposed in this paper; (c) the imaging result of the six ships by the method proposed in this paper.

The contributions of this paper are summarized as follows. We develop a new SAR imaging method for directly processing the raw data via CS and analyze the SNR in the echo signal to show the feasibility of the proposed imaging method. Experimental results are provided to validate the SNR analysis, and show the superior performance of the proposed method over the traditional matched filtering methods.

Further work will be done to explore the extension of the observation model to other SAR modes (e.g., the spotlight SAR). Besides, as the SNR analysis we discussed is mainly focused on the thermal noise, the error introduced by discretization will be included in the SNR analysis. The accelerated recovery algorithm will be addressed. As is mentioned in Section 3, the proposed method needs to construct the measurement matrix of which the size is in square order to the size of the target vector. Meanwhile, the proposed method also requires more computational efforts to obtain the radar image since it needs multiplication of the measurement matrix with the estimated target scene. The optimization of the recovery algorithm is currently in progress, and will be presented elsewhere.

Acknowledgements

This work was supported by State Key Development Program for Basic Research of China (Grant No. 2010CB73-1905).

References

1 Curlander J C, McDonough R N. Synthetic Aperture Radar: Systems and Signal Processing. Hoboken: John Wiley & Sons Inc, 1991
2 Cumming I G, Wong F H. Digital Processing of Synthetic Aperture Radar Data: Algorithms and Implementation. MA: Artech House Inc, 2005
3 Raney R K, Runge H, Bamler R, et al. Precision SAR processing using chirp scaling. IEEE Trans Geosci Rem Sens, 1994, 32: 786–799
4 Donoho D L. Compressed sensing. IEEE Trans Inform Theor, 2006, 52: 1289–1306
5 Candès E J, Tao T. Near-optimal signal recovery from random projections: universal encodeing strategies. IEEE Trans Inform Theor, 2006, 52: 5406–5425
6 Candès E J, Romberg J, Tao T. Stable signal recovery from incomplete and inaccurate measurements. Comm Pure Appl Math, 2006, 59: 1207–1233
7 Baraniuk R G, Steeghs P. Compressive radar imaging. In: IEEE Radar Conference, Boston, 2007. 128–133
8 Ender J H G. On compressive sensing applied to radar. Signal Process Spec Sec Statis Signal Array Process, 2010, 90: 1402–1414
9 Patel V M, Easley G R, Healy J, et al. Compressed synthetic aperture radar. IEEE J Sel Top Signal Process, 2010, 4: 244–254
10 Zhang B C, Jiang H, Hong W, et al. Synthetic aperture radar imaging of sparse targets via compressed sensing. In: 8th EuSAR, Aachen, 2010. 1–4
11 Alonso M T, Dekker P L, Mallorquí J J. A novel strategy for radar imaging based on compressive sensing. IEEE Trans Geosci Rem Sens, 2010, 48: 4285–4295
12 Herman M A, Strohmer T. High-resolution radar via compressed sensing. IEEE Trans Signal Process, 2009, 57: 2275–2284
13 Lin Y G, Zhang B C, Jiang H, et al. Multi-channel SAR imaging based on distributed compressive sensing. Sci China Inf Sci, 2012, 55: 245–259
14 Candès E J, Tao T. Decoding by linear programming. IEEE Trans Inform Theor, 2005, 51: 4203–4215
15 Mallat S, Zhang Z. Matching pursuit with time-frequency dictionaries. IEEE Trans Signal Process, 1993, 41: 3397–3415
16 Tropp J A, Gilbert A C. Signal recovery from random measurements via orthogonal matching pursuit. IEEE Trans Inform Theor, 2007, 53: 4655–4666
17 Daubechies I, Defriese M, DeMol C. An iterative thresholding algorithm for linear inverse problems with a sparsity constraint. Comm Pure Appl Math, 2004, 57: 1413–1457
18 Beck A, Teboulle M. A fast iterative shrinkage-thresholding algorithm for linear inverse problems. SIAM J Imag Sci, 2009, 2: 183–202
19 Candès E J, Wakin M. An introduction to compressive sampling. IEEE Signal Process Mag, 2008, 25: 21–30
20 Hennenfent G, Herrmann F J. Simply denoise: wavefield reconstruction via jittered undersampling. Geophysics, 2008, 73: 19–28
21 Aeron S, Saligrama V, Zhao M. Information theoretic bounds for compressed sensing. IEEE Trans Inform Theor, 2010, 56: 5111–5130